

High-Pressure Nonequilibrium Dynamics on Second-to-Microsecond Time Scales: Application of Time-Resolved X-ray Diffraction and Dynamic Compression in Ice

HPSTAR
1223-2021

Chuanlong Lin and John S. Tse*



Cite This: *J. Phys. Chem. Lett.* 2021, 12, 8024–8038



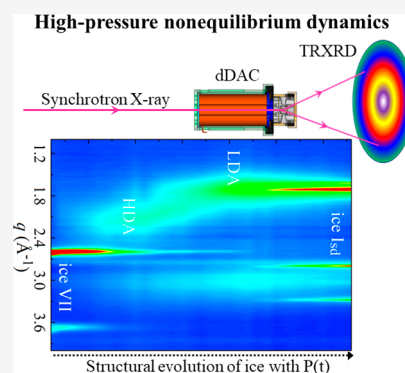
Read Online

ACCESS |

Metrics & More

Article Recommendations

ABSTRACT: The study of nonequilibrium transition dynamics on structural transformation from the second to microsecond regime, a time scale between static and shock compression, is an emerging field of high-pressure research. There are ample opportunities to uncover novel physical phenomena within this time regime. Herein, we briefly review the development and application of a dynamic compression technique based on a diamond anvil cell (DAC) and time-resolved X-ray diffraction (TRXRD) for the study of time-, pressure-, and temperature-dependent structural dynamics. Applications of the techniques are illustrated with our recent investigations on the mechanisms of the interconversions between different high-pressure ice polymorphs. These examples demonstrate that a combination of dynamic compression and TRXRD is a versatile approach capable of providing information on the kinetics and thermodynamic nature associated with structural transformations. Future improvement of rapid compression and TRXRD techniques and potentially interesting research topics in this area are suggested.



Pressure is an important thermodynamic variable for driving chemical and physical changes in materials. Compared to temperature, pressure can be generated in a broad range conveniently in the laboratory, from ultralow vacuum (or even negative pressure by tension) to hundreds of GPa (e.g., in opposing diamond anvils), spreading over 20 orders of magnitude.¹ External compression forces the atoms in the materials closer together and modifies the chemical bonds. This may be explained simplistically with the particle-in-a-box model.² The reduction of the linear dimensions of the confinement potential raises the energy level. This leads to the mixing of occupied valence orbitals with often spatially extended and unoccupied orbitals for an atom. On the one hand, orbital rehybridization alleviates the Pauli repulsion between electrons and provides orbital flexibility for chemical bonding. The change in the nature of chemical interactions often leads to structural transformation. An early example is the pressure-induced transformation of face-centered cubic (fcc) elemental cesium at around 4 GPa,³ later suggested as a result of a $s \rightarrow d$ transition.⁴ Chemically, this is equivalent to the hybridization of the Cs valence 6s with the empty 5d orbitals. Overlaps between the diffuse 5d orbitals help to delocalize the electrons and resulted in a sequence of structural changes. Within a small pressure interval, the structure changed from face-centered cubic (fcc) to a complex orthorhombic ($C222_1$), and then, to a body-center phase tetragonal ($I4_1/amd$) structure.⁵ In the latter, the valence electron distribution was found to be sinusoid wave-like and

intercalated between the atomic layers throughout the entire crystal structure.⁶ Orbital hybridization is critical to structural transformation and the associated change in physical and electronic properties. Early research in high-pressure science focused on investigating equilibrium thermodynamics, measuring the physical and electrical properties, and identifying the structure of the transformed phases.

There were several important breakthroughs in instrumentation in the late 1970s and 1980s.^{1,7–11} The first is the significant improvement in the design of the diamond anvil cell (DAC) and the development of auxiliary spectroscopic characterization techniques.^{12,13} The diamond anvil cell is a simple device where pressure can be generated by confining a small amount of materials in a gasket sandwiched between two opposing diamonds with flattened faces. Second, the advancements and general availability of collimated, tunable, and intense synchrotron radiation has improved.^{1,7–11} The combination of both has led to a revolution in high-pressure science.¹ X-ray diffraction studies that emerged in the late 1990s and early 2000s have revealed the richness of (new) structural types and the complexity of high-pressure poly-

Received: May 22, 2021

Accepted: August 10, 2021

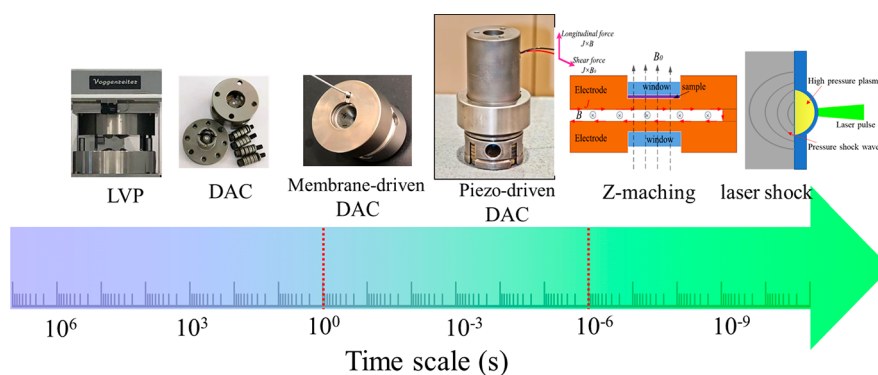


Figure 1. Schematic of the time regimes relevant to pressure-induced phase transitions with different loading methods. Images reprinted with permission from refs 1, 24, and 25.

morphs of simple elements.^{9,14} To this day, mechanisms for some of the phase transformations are still unknown, and it remains a topic of active research. Structural changes will lead to new physical and electronic properties. Augmented by the availability of accurate electronic structure and structural prediction software in recent years, many peculiar properties were predicted and found.¹⁵ A topical example is the recent synthesis of polyhydrides with superconducting behavior close to room temperature,^{16–18} albeit at very high pressures. On a more practical note, the high-pressure state has recently been exploited as a synthetic tool for novel metastable materials.¹⁹ Therefore, the subject of structures, structural transformations, and mechanisms are related and highly relevant.

Phase transition can be classified as displacive or reconstructive.^{20,21} Displacive transition involves the cooperative motion of a relatively large number of atoms, each being displaced by only a small distance relative to its neighbors. A reconstructive transition involves substantial reconstruction of the crystal and rearrangement of the atoms. This will involve the breaking and formation of chemical bonds associated with an energy barrier for the transformation. Furthermore, there is no topological and group–subgroup relationship in the crystallographic orientation between the product and the precursor.²¹ In either mechanism, the atom movements often follow the minimum-energy path to the product in response to compression. Under this condition, there is no guarantee that the product is in the thermodynamic ground state. Heating may help to overcome the activation energy leading to a more stable structure. Nevertheless, structural transformation is associated with the displacement and rearrangement of atoms. The minimum time for a structural change to occur is expected within picoseconds to femtoseconds, corresponding to the time scale of translational vibrations in a solid. Displacive transformations usually have low activation energies and are relatively rapid. A reconstructive transformation is often associated with large activation energy and is generally sluggish. In a dynamic shock wave experiment, the structural phase transition is generally in the order of nanosecond or shorter (Figure 1). In comparison, static compression is diffusion-limited, and the time scale is millisecond to microsecond, or sometimes even from minutes to days, depending on the loading (strain rate) and the activation barrier. It is not unusual to observe different products from the same material by static and dynamic shock waves. This is because the transformation is not necessarily a thermodynamic process. It is governed by kinetics involving nonequilibrium (transient or metastable) intermediate state. Many factors,

including the strain rate, temperature, pressure, nucleation, defect formation, will contribute to the transformation rate. These effects are significant in the intermediate time scale regime from microsecond to a second (or minute). The experimental techniques to promote and to access information on phase transitions at different times can be roughly divided into three regimes (Figure 1). For time under a microsecond, shockwaves produced by high kinetic energy impact or laser shock can be probed by a short X-ray pulse from a free-electron laser.²² Conventional static compression (*e.g.*, large volume press, LVP, and DAC) and detection methods can be used to study processes longer than seconds. The intermediate time regime, between microsecond to second, can now be accessed with rapid pressure loading, as described below. This Perspective focuses on recent studies on the rate-dependent transformation kinetics with different pressure (dynamic) loading rates. The purpose is to investigate the nature of the nonequilibrium state of materials upon rapid compression/decompression processes in the intermediate time regime.^{23,24}

Instrumentation. Overcoming the two technical challenges of controlling rapid compression and detecting X-ray patterns quickly is essential for studying the structural evolution of material phase transitions in intermediate time (Figure 1). The first problem was resolved with the improved design and automation of the dynamic diamond anvil cell (dDAC).^{24,26–28} The availability of noise-free hybrid photon counting (HPC) large-area detectors allows accurate determination of the scattering angles and diffraction intensities over a large dynamic range at frame rates of kilo-hertz (up to 4000 patterns per second) or less.^{23,27} The introduction of the HPC detector has radically transformed X-ray diffraction experiments at the synchrotron. Recently, the dDAC experiments have become possible in the X-ray free-electron laser with MHz detector, which offers more opportunities to explore the high-pressure nonequilibrium dynamic nature on the microsecond time scale.²⁹

The dynamic compression technique was designed to study the kinetics of phase transitions and metastable phases by applying a programmable and repetitive time-dependent loading/unloading pressure profile to the DAC.^{26,30} At present, there are two main approaches to varying the pressure rapidly.^{24,26} The first one is the use of a pneumatic diaphragm (membrane) compressed with inert gas, such as helium and argon. The second method is by a piezoelectric actuator. According to experimental requirements, these two methods can be used in combination to provide loading rates at different time scales. The membrane drive consists of two

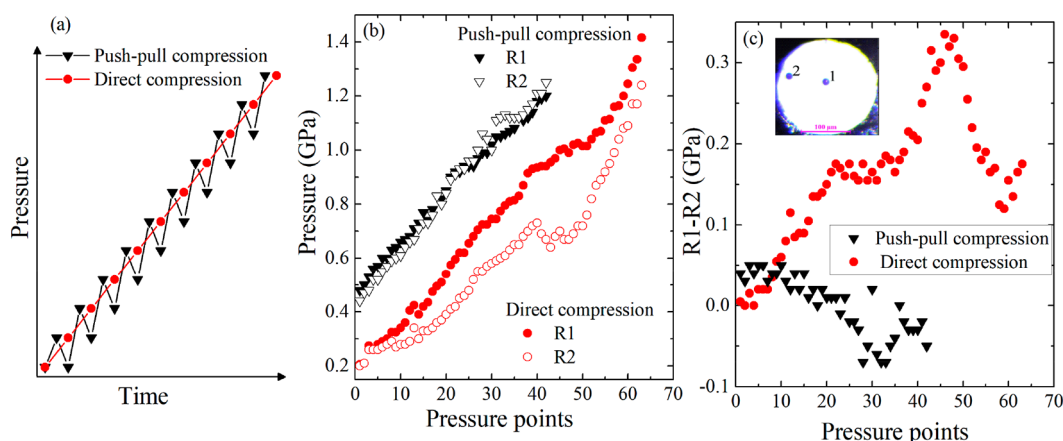


Figure 2. (a) Programmed pressure–time profile on the compression of ice Ih with the direct and push–pull modes using a double membrane-driven DAC with one pneumatic membrane on one side for compression (push) and the other for decompression (pull). (b) Pressure measurements in direct compression and push–pull compression modes at 100 K. The sample pressure was determined from the fluorescence spectra of two ruby spheres with one placed in the center (R1) of the sample chamber and the other situated close to the edge (R2) of the gasket (insert of Figure 2c). (c) The measured pressure differences in direct compression and push–pull compression modes. The push–pull compression data was adapted from ref 49.

identical thin steel sheets that can be plastically and elastically expanded by adjusting the gas pressure applied to the pneumatic diaphragms.²⁴ Pressure loading to the DAC is achieved by expanding/contracting the membranes for the compression/decompression process, which can be controlled at a specific rate. A piezoelectric actuator is used for pressure modulation. It loads/unloads pressure to a DAC by increasing the voltage to the actuator controlled by a dedicated power supply, thus elongating the ceramic.²⁶ The voltage for driving the ceramic is in the range of 0–1000 V for the reported piezoelectric actuator. Two different designs have been used, either on a 1-piezo-driven or a 3-piezo-driven DAC. A newly developed 1-piezo (or 3-piezo)-driven DAC can provide a loading rate up to 160 TPa/s repeatedly over a 100 GPa pressure range.²⁷ Since the piezo-driven DAC was first used in early 2000 to study time-dependent phenomena under high pressure, it is commonly known as dynamic diamond anvil cell (dDAC).²⁶

Since the inception of the first dDAC, there have been many modifications and improvements to suit different purposes, such as high-temperature operation and increasing the compression rate.^{24,31} In the past decade, the dynamic compression in the intermediate time scales has been used to investigate time-dependent high-pressure nonequilibrium dynamics, observing diverse physical phenomena. These include compression-rate kinetics,^{30,32,33} formation of metastable phases,^{34–42} crystal growth,^{43–46} chemical reaction,⁴⁷ and strain and stress.⁴⁸ Relevant to the experiments that will be discussed below (*vide supra*) is the use of the double-membrane so the pressure can be systematically applied and reduced to control the compression and decompression processes at different rates.²⁴ Apart from the convenience of pressure adjustment under cryogenic conditions in an enclosure, the additional diaphragm provides the flexibility of fine pressure tuning to mimic a quasi-hydrostatic condition when operated in the “push–pull” mode.⁴⁹ In the example shown in Figure 2, the ice sample in a DAC was first compressed in a small pressure increment of ~ 0.04 GPa and then reduced by ~ 0.02 GPa. The repetitive back-and-forth motion of the diaphragms effectively reduced the deviatoric stress on the sample, as demonstrated by the minimal pressure

difference between the ruby ball located at the center of the DAC and ruby ball near the edge of the gasket hole.⁴⁹ A comparison between push–pull compression and direct compression shows the former can provide a better hydrostatic environment (Figure 2b,c).

Synchrotron radiation, especially from third-generation sources, provides high-energy, high-flux, low-emittance, and micrometer-sized X-ray beams that can penetrate small samples through the surrounding vessel materials with high intensity and spatial resolution.^{50–55} The high brilliance and short-pulsed timing structure of the synchrotron X-ray beam are essential for some time-resolved X-ray diffraction experiments, *e.g.*, investigating transient phenomena at extreme conditions from seconds to nanoseconds. The recent adaptation of detector technology from high-energy physics, such as the DECTRIS²³ and LAMBDA large-area detectors,²⁷ can attain the measurement of angular resolved X-ray diffraction patterns at a repetition rate up to 4 kHz. Combined with the dDAC, the advancement in instrumentation and software for dynamic pressure control, X-ray data collection, and pattern analysis have enabled the study of the structural changes of dynamic processes in the millisecond time scale, *e.g.*, time-dependent kinetic pathways of phase transformation, stress relaxation, nonequilibrium phenomenon, and chemical reaction under extreme pressure–temperature conditions. Lately, several beamlines have been constructed specifically for time-resolved X-ray diffraction measurements, for example, the nanosecond time resolution beamline at the Dynamic Compression Sector of Advanced Photon Source (APS)⁵⁶ and submillisecond time resolution beamline at sector-16 HPCAT of APS²³ and the Extreme Conditions beamline at Petra III.⁵²

Kinetic Analysis. Information about the energy landscape, transformation kinetics, and mechanism can be extracted by analyzing the results from time-resolved compression and decompression experiments. In a high-pressure experiment, the initial phase (*e.g.*, phase A in Figure 3) is pressurized across the equilibrium phase boundary and exists as a metastable phase. The occurrence of a phase transition depends on the competition between the driving force (*i.e.*, the difference of the Gibbs free energy, $\Delta G(P)$), temperature, and intrinsic energy barrier (Figure 3). The transition kinetics is the

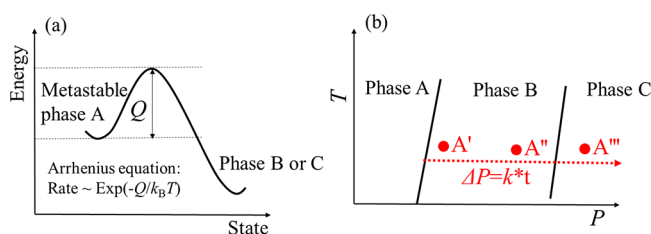


Figure 3. (a) Energy landscape for the transformation kinetics. (b) Rate-dependent overpressurization under rapid compression.

combined result of nucleation, growth, and impingement. The rate for nucleation and crystal growth often follows the Arrhenius equation (Figure 3a),^{22,57–59} *i.e.*, the rate = $C_0 \exp[-Q/k_B T]$, where C_0 is a constant related to the jump frequency of atoms and Q is the nucleation energy barrier (Q_N) or growth energy barrier (Q_G). At constant P – T (*e.g.*, at the point A'), the activation energies for both nucleation and growth are assumed to be constant. The extent (or fraction) of the product phase in the phase transition can be described as a function of time by the Johnson–Mehl–Avrami–Kolmogorov (JMAK) equation.^{59,60} The transformation rate, *viz.*, the inverse of the characteristic time, follows the Arrhenius equation, $1/\tau \sim \exp[-Q_{ave}/k_B T]$, where Q_{ave} is an average energy barrier in the entire transition kinetic process with nucleation and growth. This quality can be determined by fitting the experimental τ – T data to the Arrhenius equation.

If the applied pressure (P) changes linearly with time (t) by a constant increment rate (k), *i.e.*, $P(t) = kt$, the energy barrier will also change with time (or pressure). Suppose the onset transition pressure is defined by the initial nucleation step for homogeneous nucleation. Then, the critical nucleation energy barrier is proportional to $\gamma^3/\Delta G(P)^2$, where γ is interfacial energy related to the structures of parent and product phases and $\Delta G(P)$ is the pressure-dependent difference in the Gibbs free energy. When the overpressure is small (for example, at point A' , Figure 3b), $\Delta G(P)$ is large, leading to a high critical nucleation energy barrier and low nucleation rate (or probability) for the phase transformation at point A' . It also will result in a slow growth rate of the new phase and a long transition time. When the pressure loading time (high compression rate) is much shorter than the nucleation rate, the metastable phase A can be overcompressed. For example, under rapid compression at a ramp rate, phase A may coexist with phase B at point A'' . At this point, $\Delta G(P)$ is very large and leads to a lower energy barrier allowing a thermally driven transition to occur in a short time scale. The transition mechanism would then change from thermally driven homogeneous nucleation to dislocation nucleation. Another case is when phase A is overcompressed to point A''' under rapid compression (Figure 3b). In this case, the interfacial energy due to the mismatch between the phase A and C structures will be large. Then, phase A may transform to an intermediate state first with a smaller γ with a lower transition energy barrier. Previous studies show that the interface energy between crystal and liquid (or crystal and glass) display small values.^{59,61} If this is the case, pressure-induced amorphization or metastable melting can occur.^{62–64}

Another piece of useful information that can be obtained from a time-resolved experiment is the compression-rate-dependent energy barrier. It is possible to show qualitatively that the activation barrier is a function of pressure. Previous studies have shown that for a given compression rate there is a

corresponding specific effective (or average, Q_{ave}) energy barrier and onset transition pressure.³⁰ The compression rate often exhibits an exponential relationship between T and Q_{ave} . If the experiments are conducted at different compression rates at several temperatures, Q_{ave} can be characterized as a function of the transition pressure. The activation volume (ΔV) is obtained from the derivative of the activation energy with pressure, *i.e.*, $\Delta V = dQ_{ave}/dP$, and reflects the sensitivity of the transformation barrier of the nucleation and growth process to pressure. The larger ΔV is, the more effective is the pressure to decrease the activation energy for the phase transition.

Applications. Since the inception and fabrication of the dDAC in the early 2000s,²⁶ many innovative modifications and improvements have greatly expanded its utility.^{23,24,27,28,31} The dynamic loading technique has been used to study a variety of problems and has provided insightful results. This technique has been applied to the study of a wide range of high-pressure phenomena. The following examples illustrate a few applications. Earlier on, structural changes of the sample were monitored by visual observation complemented with Raman spectroscopy. In this way, the compression-rate dependence on the local order in the crystallization of water to ice VII,³² the transformation pathways between the ice phases,³⁶ ice to supercompressed water,⁴³ and crystal growth rates in hydrogen and deuterium⁴⁴ were investigated. Later, the dDAC was coupled to time-resolved X-ray diffraction with synchrotron radiation. This progress opens a new *in situ* tool to characterize the kinetics and structures of phase transitions at different time scales. The first study was on the effect of the compression rates on the solidification of liquid krypton and the subsequent face-centered cubic (fcc) to hexagonal (hcp) phase transition in solid krypton at room temperature.⁴⁵ The results show the strong influence of the compression rates on the liquid-to-solid transition, but it has an almost negligible effect on the solid–solid transition. The relative temporal amount of the liquid and the solid phase can be estimated from the area ratio underneath the respective characteristic diffraction features. It was then found the calculated relative concentrations fit well to the Johnson–Mehl–Avrami–Kolmogorov equation (*vide supra*) with an Avrami constant of 1,⁶⁰ which suggests the liquid-to-solid nucleation is spontaneous with a nucleation time of ~ 0.12 – 0.18 s. This experiment demonstrated the potential of TRXRD to provide valuable kinetic and mechanistic information on phase transformation. An interesting discovery is the observation of a metastable liquid melted from a high-pressure crystalline polymorph of bismuth (Bi-IV) under quasi-hydrostatic decompression.⁶⁴ The possible existence of a transient liquid in a solid–solid transformation was proposed to explain some of the usual behavior in metal alloys and amorphous ices.^{62,63,65,66} In a recent experiment, *in situ* time-resolved X-ray diffraction patterns of a Bi-IV were recorded from decompression close to but under the melting point under quasi-hydrostatic conditions using a double membrane-driven DAC (*vide supra*).⁶⁴ When Bi-IV is decompressed at 4 GPa, the crystalline diffraction pattern transformed to an amorphous-like pattern at 2.3 GPa and eventually crystallized to Bi-I at 1.2 GPa. Compared to the crystal diffraction patterns measured from the compression of Bi-I at the same temperature, this suggests that the amorphous-like phase in the decompression may be attributed to a metastable liquid melted from a crystalline solid below the melting temperature. This is tantalizing but nonconclusive evidence as further

experiments are needed to verify the interpretation. In this Perspective, we will give a synopsis of our experience of TRXRD with dynamic loading, drawing on recent examples exploring the ice phase diagram.

Water is a common and well-studied material, but it exhibits many anomalous properties that are still not fully under-

Water is a common and well-studied material, but it exhibits many anomalous properties that are still not fully understood.

stood.⁶⁷ There is a vast collection of literature on this subject. A problem of topical interest is the structural inter-relationship between water and supercooled water and the underlying crystalline and amorphous ices.⁶⁸ Liquid water can be cooled to -48.3 °C before homogeneous nucleation to ice occurs. However, when it is cooled very quickly (10^6 K/s), the crystal nucleation is avoided and water becomes a glass with a glass transition temperature believed to be around 136 K.^{69–71} In comparison, crystalline ice can be compressed to a dense amorphous form (HDA) at low temperature (e.g., <100 K).⁷² Heating the compressed sample at constant pressure (at ca. 160 K and 1–2 GPa) resulted in an even higher density disordered form (VHDA).⁷³ On the other hand, decompression of HDA at 77 K did not revert to the precursor crystalline ice, but it led to a low-density amorphous form (LDA) that can be recovered at ambient pressure.⁷⁴ On slow decompression, X-ray and neutron diffraction have found that the HDA-to-LDA transformation is not discontinuous but via several metastable amorphous structures.⁷⁵ Furthermore, depending on the pressure and heating rate, HDA can transform into different high-pressure ice polymorphs.⁷⁶ These observations raised the obvious questions, are amorphous ices and liquid water (normal and supercooled) connected? If so, how does the structure mutate from the solid to the liquid phase? Can we explain the anomalies of the liquid from the different structures of the amorphous forms? Many theories and hypotheses have been suggested to rationalize these phenomena.^{77–80} Although there is no definitive answer right now, one thing is certain: the ease of structural transformations among the amorphous states and between amorphous and crystalline ices shows the energy barriers between various forms are low. Thus, the kinetics and product are sensitive to the heating and/or compression–decompression rates. Conversely, one can survey the energy landscape of the amorphous and crystalline states from the structures by adjusting the temperature and pressure parameters systematically using TRXRD and dynamic loading/unloading.

Figure 4 shows the metastable P – T phase diagram of water/ice. When water is cooled, the thermodynamically stable crystalline state is ice Ih. When ice Ih is compressed at $T < 100$ K, it transforms to HDA ice at around 1 GPa.⁷² The release of pressure converts HDA to LDA at 77 K.⁷⁴ When compressed at room temperature, water crystallizes to ice VI at ca. 0.8 GPa and then to ice VII at 2.2 GPa. Hydrogen-ordered ice VIII is formed when cooled below 280 K. However, liquid water can be supercooled at ambient pressure to -48 °C (224 K). Below this temperature, it spontaneously nucleates to crystalline ice. It was then speculated that the supercooled liquid could be extended to low temperature into the glass transition

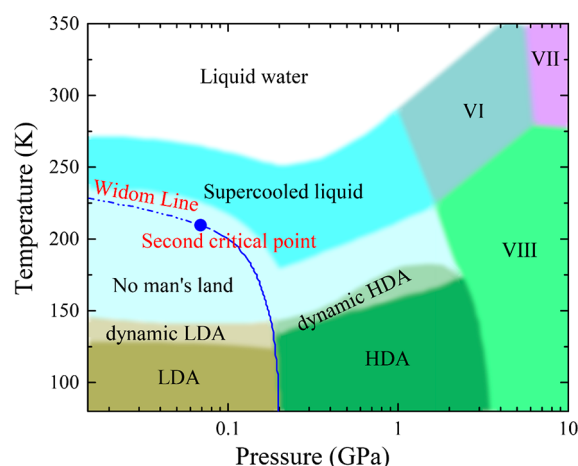


Figure 4. P – T phase diagram of water/ice showing the thermodynamic stable crystalline high-pressure polymorphs and the amorphous phases, LDA, and HDA.^{70,78–84}

temperature of the amorphous ice, estimated to be at 136 K.^{69–71} However, the hypothesis cannot be tested directly experimentally in this part of the phase diagram. This region of the phase diagram is known as water's no man's land.⁶⁹ The multifaceted polyamorphism between metastable phases is a clear sign of the kinetic nature of the transformations. With the richness of the water/ice phase diagram and a fundamental interest in understanding water, it was the first subject studied by the new dynamic compression/decompression technique. A surprising finding is the formation of HDA from metastable ice VII under rapid compression of liquid water in the stability field of ice VI.

A common route (top-down) to reach no man's land is to rapidly cool bulk water or emulsified water droplets⁸⁵ and examine the structures with spectroscopic or diffraction methods at ambient pressure. A recent ultrafast X-ray scattering has probed supercooled bulk water at 227 K in the water's no man's land for a few milliseconds.⁸⁶ We adopted a bottom-up strategy to enter no man's land from the amorphous phase by controlling the kinetics. Crystalline ice Ih was first compressed to HDA at desirable pressures. The sample was then heated *in situ* at constant pressure at defined rates. Decompression experiments starting at selected pressure and temperatures were also performed. The associated structural changes were monitored by TRXRD.

The first problem to address is the mechanism of the pressure-induced amorphization of crystalline ice and whether the amorphized HDA is related to quenched water. Initially, it was suggested that the transformation of ice Ih to HDA at low temperature is a process similar to melting and is thermodynamically connected to the melting line extrapolated from the freezing point to low temperature.⁶⁹ If this is correct, the amorphous form is a genuine representation of quenched water. Another interpretation is that it is due to a mechanical instability that is controlled by kinetics.^{87–90} In this case, the crystal-to-amorphous transition will depend on the hydrostaticity of the environment, the compression temperature, and the loading rate.

Because deuterium has a large neutron coherent-elastic cross-section favorable for diffraction studies, early structural investigations of pressure-induced amorphization (PIA) of ice were mostly performed with neutron scattering. Before the availability of spallation neutron sources, it often took hours to

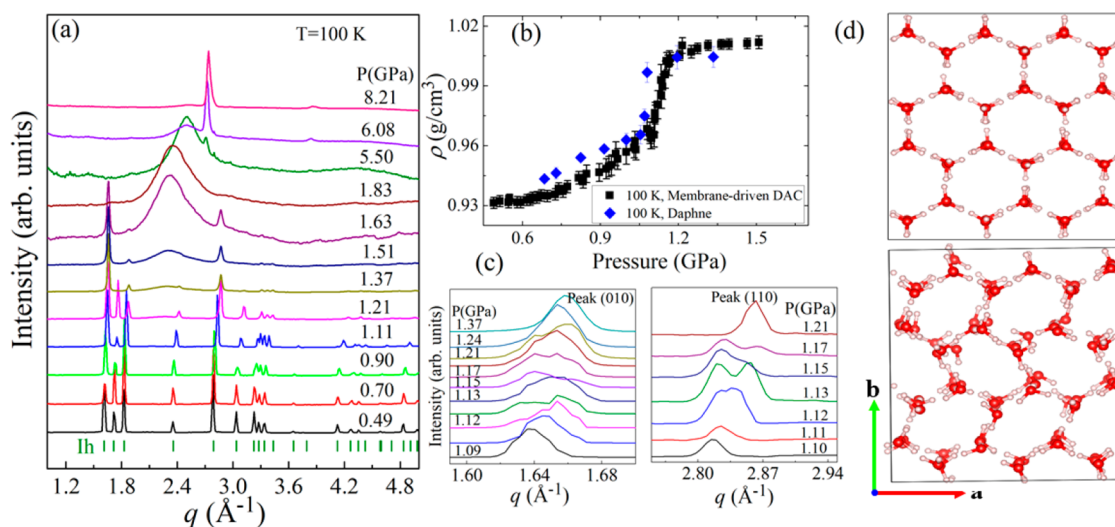


Figure 5. (a) X-ray diffraction patterns of ice compressed at 100 K. (b) Calculated densities of the sample at different pressures. (c) The splitting of the (010) and (110) Bragg peaks. (d) Schematic illustration of the shear distortion obtained from molecular dynamics calculations. Adapted with permission from ref 49. Copyright 2017 American Physical Society.

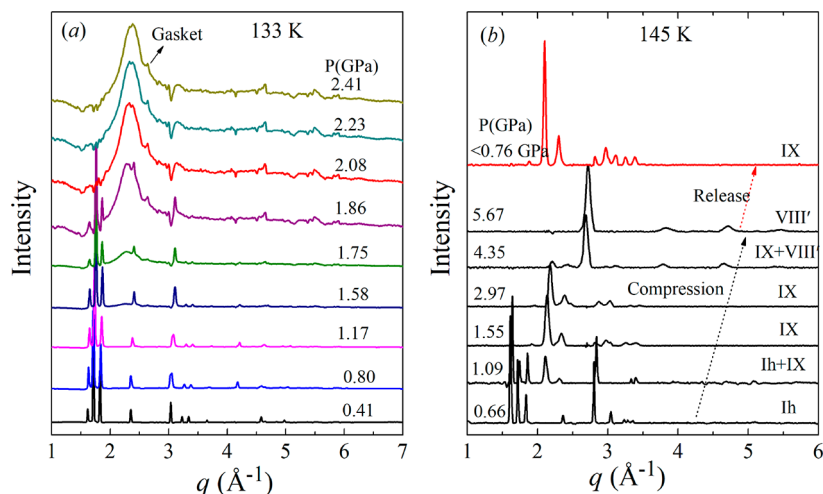


Figure 6. X-ray diffraction patterns of ice Ih compressed at 133 and 145 K under quasi-hydrostatic conditions with a pressure medium Daphne 7474. Adapted with permission from ref 49. Copyright 2017 American Physical Society.

record a diffraction pattern and time-resolved studies were rare. The main advantage of neutron diffraction is a large ice sample (mm^3) wrapped in an indium cup to create quasi-hydrostatic conditions.⁷⁴ However, because of the time constraint, pressure increments were nonuniform and often in fairly large steps. In this aspect, X-ray diffraction using the push-and-pull processes is more efficient.

Our first study was the examination of the ice structure upon compression and decompression at 100 K.⁴⁹ A neat sample was compressed in a small pressure increment of ~ 0.04 GPa and then reduced by ~ 0.02 GPa in each step at a loading rate of < 0.01 GPa/s. The measured diffraction patterns are shown in Figure 5a. Similar patterns and pressure trends in densities were observed on a sample in a pressure-transmitting medium Daphne 7474 (Figure 5b). The results show a sudden onset of densification around 1.2 GPa. However, immediately before the structural transformation, the (010) and (110) Bragg reflections (Figure 5c) belonging to ice Ih were found to split, indicating a distortion of the crystalline lattice. This intermediate phase is found to be short-lived, between 1.10

and 1.26 GPa. The distortion is likely due to a shear instability predicted earlier (Figure 5d).^{87,91} Complete conversion to the amorphous form was achieved at pressures higher than 1.87 GPa (Figure 5a). Upon further compression to 5.5 GPa, a single peak corresponding to an ice VII-like structure (ice VII/ice VIII') emerged, and eventually, a pure crystalline form was observed at 8.21 GPa. The stability field of the HDA observed in this experiment is between 1.3 and 8 GPa. Next, we studied the temperature effect on the PIA transition. The diffraction patterns at 133 and 145 K are shown in panels a and b of Figure 6, respectively. Amorphization was observed at 133 K. When compressed at 145 K, ice Ih converted successively to ice IX and then to ice VIII'. This is the expected "normal" crystal-to-crystal transformation sequence,⁹² as the crystalline forms are the stable thermodynamic states at these pressure-temperature conditions. The results indicate PIA is a kinetic process and sensitive to temperature.

The reverse decompression experiments support the metastability of the amorphous states. The experimental X-ray diffraction patterns upon pressure release of the amorphous

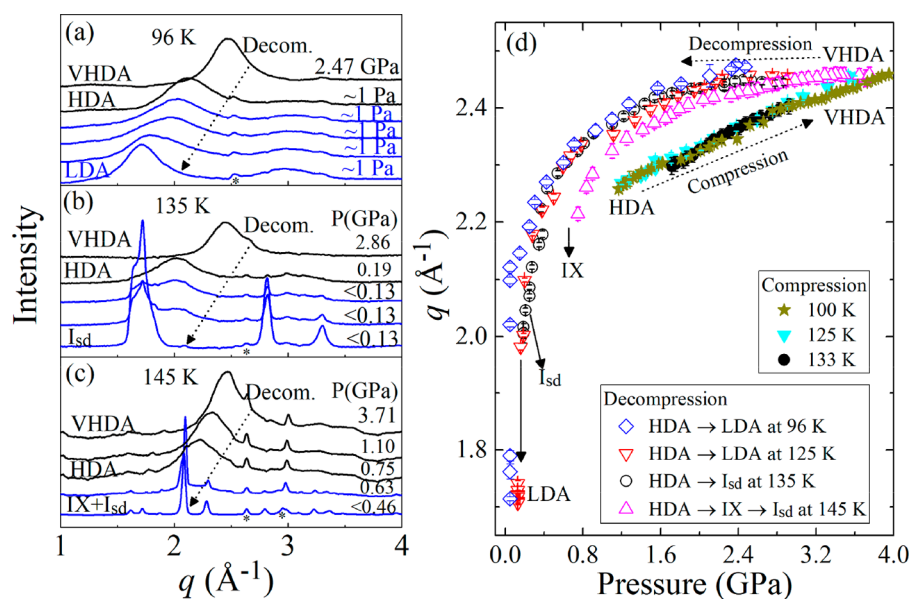


Figure 7. Structural evolution of amorphous ice under decompression (a) at 96, (b) at 135, and (c) at 145 K. Amorphous ice at 145 K was obtained by heating VHDA from 133 to 145 K. (d) The first sharp peak position (Q) of amorphous ices as a function of pressure. Adapted with permission from ref 49. Copyright 2017 American Physical Society.

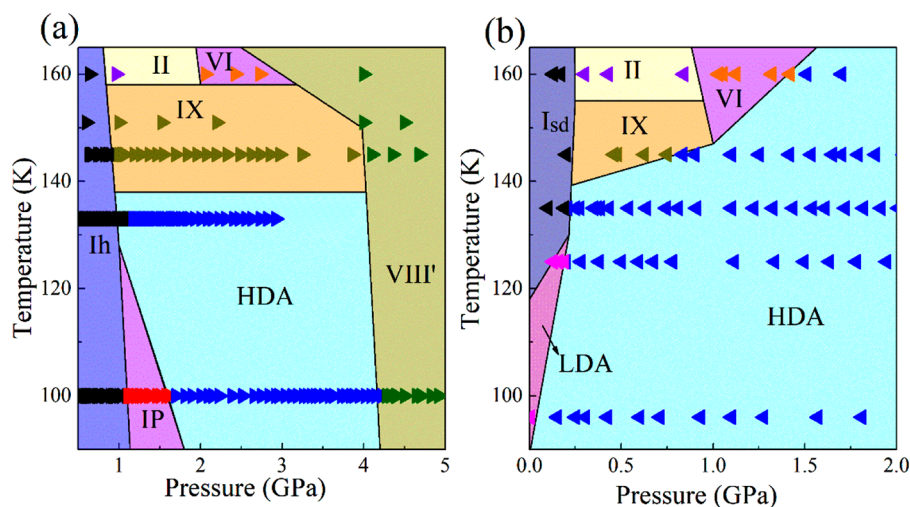


Figure 8. “Phase” diagram constructed from diffraction information for (a) slow compression of ice Ih and (b) slow decompression of amorphous ice. Adapted with permission from ref 49. Copyright 2017 American Physical Society.

ices at 96, 135, and 145 K are compared in Figure 7. The diffraction patterns show different transformation sequences at different temperatures. At low temperature (96 K) the previously reported very high-density amorphous (VHDA) \rightarrow HDA \rightarrow LDA sequence was found. The observations reflect a relaxation effect. The formation of VDHA⁷³ can be attributed to reducing the internal stress of (kinetically) compressed HDA upon annealing. Therefore, upon the pressure release, the VHDA converted to low-density HDA and then to LDA with an ice-like structure. Because of the pressure–volume work (PV), heat is released at each step (exothermic). Because the density difference between HDA and LDA is significant, the heat released promotes the transformation, and the process becomes so fast it appears to be first-order. At 135 K, the HDA \rightarrow LDA transition terminated at a more stable stack faulting crystalline ice (I_{sd}). At a higher temperature of 145 K, the high-density amorphous ices transform to crystalline ice IX and then

to ice I_{sd} . The interpretation of the observed sequence of events is straightforward. Starting from the decompression of VHDA, at low temperature, the rearrangement of the hydrogen-bond (H-bond) network to the corresponding thermodynamic stable high-density ice in the stability field requires an activation that cannot be fully compensated by the PV work and available thermal energy. When the temperature is raised, additional thermal energy is acquired to overcome the transition barrier from LDA to ice I_{sd} . The thermal energy is still not sufficient to convert VHDA and HDA into the corresponding crystalline ice forms at this temperature. On further warming, HDA eventually transforms to ice IX.

The kinetic nature of the structural transformations among the different forms (crystalline and noncrystalline) is succinctly summarized in the “phase” diagrams constructed from the structural information obtained from X-ray diffraction on the compression and decompression processes (Figure 8). The

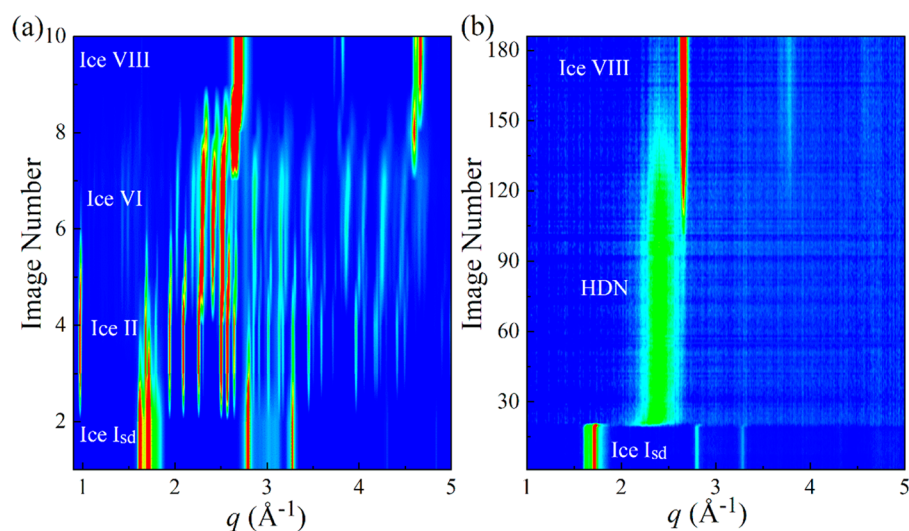


Figure 9. Diffraction patterns on the compression of ice Ic at 165 K. (a) Under slow compression (<0.01 GPa/s) from ~ 1 Pa to 5 GPa at an interval of ~ 0.05 GPa. (b) Under rapid compression from ~ 1 Pa to 3.5 GPa at a rate of ~ 14.8 GPa/s. An online ruby system monitored the sample pressure. Adapted with permission from ref 38. Copyright 2018 American Physical Society.

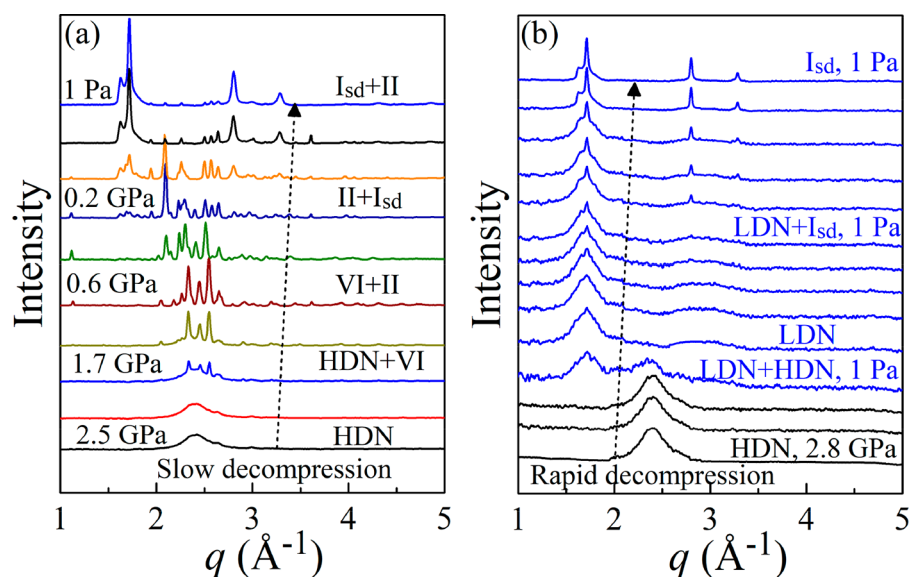


Figure 10. Rate-dependent structural transformation of HDN at 158 K under decompression. (a) Slow decompression. (b) Rapid decompression (~ 10 GPa/s) of HDN. Adapted with permission from ref 38. Copyright 2018 American Physical Society.

two phase diagrams do not mirror each other. The structures obtained at the same P – T point by compression or decompression are not the same. Therefore, either one or both structures cannot be in the thermodynamic ground state.

A subsequent study focused on the effect of pressure and compression/decompression rates on the “phase” boundary between ice/HDA and HDA/LDA transformations.³⁸ In this study, the stack faulting ice I_{sd} is the starting crystalline form obtained from decompression of ice VIII from 4 GPa to ~ 1 Pa at 180 K; it is then cooled to the desired temperatures. Figure 9 shows the time evolution of the diffraction pattern of compressed ice I_{sd} at 165 K at two loading rates, ~ 0.01 GPa/s (slow) and ~ 14.8 GPa/s (fast). In each case, diffraction patterns were collected at 50 ms intervals.

Time-resolved diffraction experiments at different loading rates were performed from 96 to 174 K. The evolution of the diffraction patterns of ice I_{sd} compressed at two very different loading rates at 165 K are shown in Figure 9. This temperature

was chosen as it is higher than the crystallization temperature T_x and is well inside no man’s land. As expected, when the ice sample was compressed slowly, successive crystal–crystal transformations in the sequence of ice $I_{sd} \rightarrow$ ice II \rightarrow ice VI \rightarrow ice VIII were observed. In comparison, during fast compression, ice I_{sd} transformed to a high-density noncrystalline phase (HDN) and then crystallized into ice VIII. HDN is used here to distinguish it from HDA that is formed below T_x . Therefore, high-pressure stable crystalline ice phases are bypassed, and instead, they form amorphous ice under nonequilibrium conditions above T_x . Similarly, time-resolved diffraction experiments were performed to monitor the structural change on releasing the pressure of the amorphous form at different rates. A representative change in the diffraction patterns at slow and fast pressure unloading is illustrated in Figure 10. There is no surprise. Slow pressure release led to consecutive transformations into the crystalline ices in the respective stability field. On the other hand, HDN

transformed to the low-density noncrystalline form (LDN/LDA) directly upon rapid decompression, and depending on the temperature, the end product is either LDA or ice I_{sd}.

As described above the energy barrier associated with the interconversion of amorphous phases can be estimated by analyzing the compression/decompression load rates with the transition pressure with the kinetic model. For example, the first stable crystalline high-pressure phase is ice II. To bypass the equilibrium crystal–crystal transition, the compression time (Δt) must be shorter than the characteristic transition time (τ) of the ice I_{sd}-to-II transition. Because this is a kinetic process, the Arrhenius equation is employed to determine the transition time (τ). The rate constant ($1/\tau$) is proportional to $\exp(-\Delta E/k_B T)$, where ΔE is the energy barrier for the phase transition and k_B is the Boltzmann constant. The thermal energy ($k_B T$) governs the probability of the water overcoming the energy barrier. The minimum time to bypass the pressure region of the stable crystalline ice II is $\Delta t = \Delta P/\beta$, where β is the compression rate. For the amorphous (noncrystalline) phase (HDN) to form, Δt must be less than τ . This means ice I_{sd} can bypass the equilibrium pressure region of ice II in a time scale shorter than the ice I_{sd}-to-II transition. Assuming ΔE and ΔP are constants, the threshold compression rate (β_c) is determined by $\Delta t = \tau$. Substituting back to the Arrhenius equation, we obtained $\beta_c = C_0 \exp(-\Delta E/k_B T_c)$, where C_0 is a constant with a unit of GPa/s. A similar argument can be applied to describe decompression kinetics. Thus, one can estimate the energy barrier by fitting the compression/decompression rates and the corresponding transition pressures to the Arrhenius equation. Good fits (red dashed lines in Figure 11) were obtained with ΔE of 24(2) kJ/mol and C_0 of 6.4×10^8 GPa/s for compression, and ΔE of 26(2) kJ/mol and C_0 of 1.3×10^{10} GPa/s for decompression.

The characteristic time of the ice I_{sd}-to-II transition (τ) as a function of temperature can be calculated based on the fitted parameters. A plot of τ versus temperature is shown in Figure

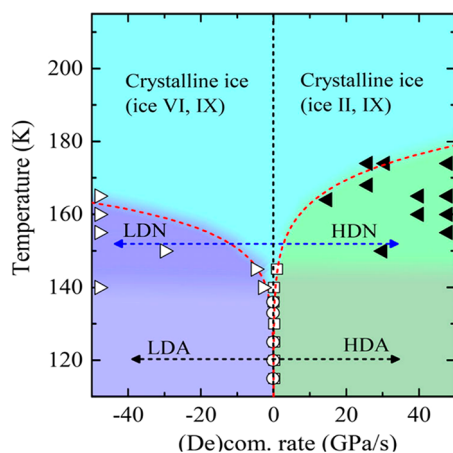


Figure 11. (De)compression-rate-dependent (negative decompression, positive compression) formation of noncrystalline phases at different temperatures. Black solid triangles represent high-density noncrystalline phases obtained by rapid compression. Open squares and circles indicate the high-density amorphous and low-density phases obtained by static compression or decompression. Open triangles are low-density noncrystalline phases formed from high-pressure ice VIII under rapid decompression. Red dashed lines are fits to the Arrhenius equation. Adapted with permission from ref 38. Copyright 2018 American Physical Society.

The combination of TRXRD and dDAC is a powerful tool in the investigation of the structural evolution of materials at various conditions under compression/decompression with different rates, providing deep insight into the underlying transition mechanism and synthesis conditions of metastable states.

12. For example, τ is estimated to be $\sim 10^7$ s for HDA formation at liquid nitrogen temperature (77 K). The time

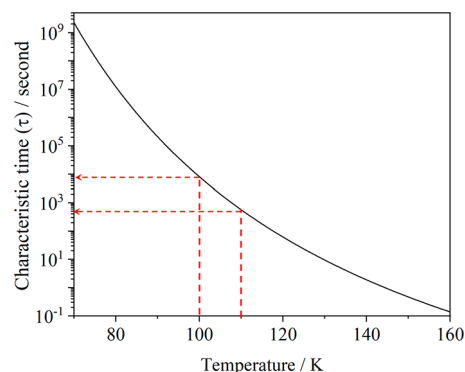


Figure 12. Change in the characteristic time (τ) for crystal-to-crystal transformation from ice I_{sd} to ice II as a function of temperature. The red lines show the characteristic time at 100 and 110 K.

shortened rapidly to 62 s at 120 K. The exponential decrease in the characteristic time with temperature may examine the discrepancy of the transformations observed in two neutron diffraction experiments with a very long relaxation time between pressure increments; apparently, both were performed at 100 K.³³ In the earlier study, a sequence of crystal-to-crystal transformations was observed. In a later investigation, even with much longer wait (annealing) times between pressure increments, the ice Ih structure was distorted preceding the transformation to HDA, as in the X-ray experiment.⁵⁴ In addition, ice VII was found to coexist with HDA at pressure as low as 1.5 GPa, indicating that ice Ih was not able to convert completely to the thermodynamically more stable crystalline form at low temperature within the experimental time. As shown in Figure 12, the characteristic time can change by more than 1 order of magnitude when the temperature is changed from 100 to 110 K. A slight error in temperature measurement can lead to dramatically different results. Experimental Raman evidence suggested HDA can be formed from dynamic compression of ice VI at 0.5 to 1.3 GPa at a compression rate up to ~ 65 GPa/s at room temperature.³⁶

A closely related issue with the poly(a)morphism of ice is whether there is a reciprocal process during the “melting” of high-density crystalline ice upon decompression. Previously, a hypothetical “melting line” between a metastable-liquid and ice VII/VIII (ice VII and VIII have a similar oxygen lattice; ice VII is the stable form above 270 K and is hydrogen disordered; the lower-temperature ice VIII is hydrogen-ordered) upon decompression was constructed from the analysis of the

phase diagram.⁹⁵ The “phase” boundary suggested that ice VIII could be recovered at 77 K at low pressure, and when heated, it might transform to an amorphous phase. The suggestions were confirmed by *ex situ* diffraction.⁹⁶ In the experiment, high-density ice was recovered at ambient pressure, annealed at several temperatures, and then cooled to 100 K for X-ray analysis. On the other hand, quasi-harmonic lattice dynamic calculations at finite temperature revealed a lattice mechanical instability,⁹⁷ similar to PIA, which also closely follows the suggested “melting line” with decreasing pressure. What is the nature of this transformation? To address this question, TRXRD measurements were performed on the metastable hydrogen-disordered ice VII. In this case, instead of varying the pressure, the time-dependent structural evolution was monitored as a function of temperature.⁴⁰

Metastable ice VII was prepared by compressing ice to ≥ 5 GPa at a given temperature between 80 and 155 K. The pressure was then released rapidly to ~ 0.5 mTorr to form metastable ice VII. The characteristic diffraction pattern confirmed the formation of ice VII. Several sets of experiments were performed at 5 mTorr. Figure 13a shows the diffraction patterns when ice VII was heated from 78 to 160 K at a rate of 0.5 K/min. The Bragg reflections of ice VII started to lose intensities at ~ 86 K. This was accompanied by the

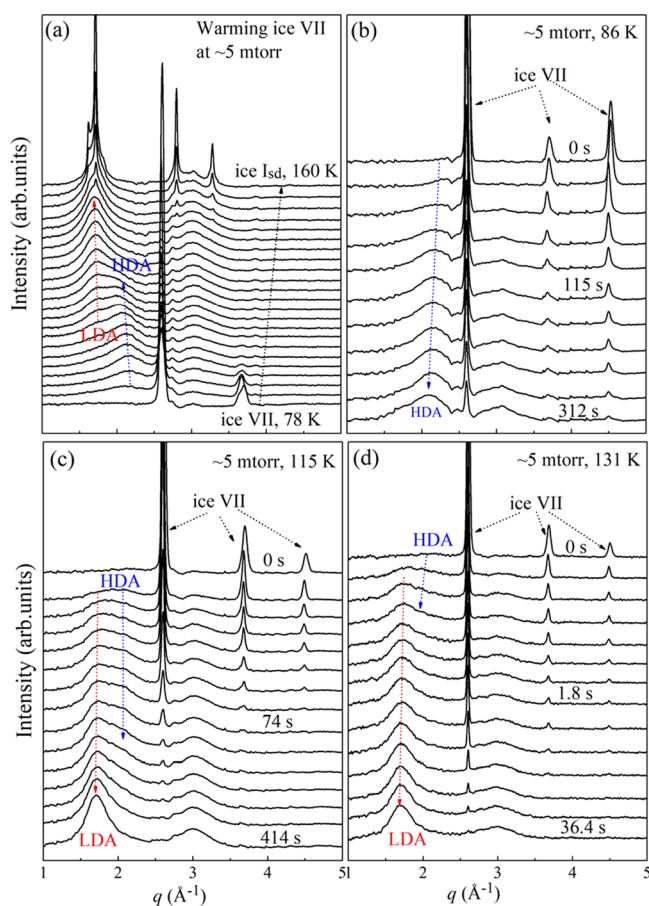


Figure 13. Structural evolution of metastable ice VII at ~ 5 mTorr. (a) Warming from 78 to 160 K at a heating rate of <0.5 K/min. (b, c, and d) The time-dependent diffraction patterns at 86, 115, and 131 K, respectively. Blue arrows indicate a broad peak of HDA with $q \approx 2.13 \text{ \AA}^{-1}$. The red arrows indicate LDA. Adapted with permission from ref 40. Copyright 2020.

simultaneous appearance of a broad peak $q \approx 2.14 \text{ \AA}^{-1}$ (blue arrow), indicating the formation of HDA. The intensity of the first sharp diffraction peak (FSDP) of HDA increased with temperature. At 107 K, a second broad peak at $q \approx 1.73 \text{ \AA}^{-1}$ emerged, signaling the presence of LDA. The relative FSDP intensity of LDA and HDA increased upon further heating. The Bragg reflections belonging to ice VII and the FSDP of HDA vanished at ~ 125 K. Above 150 K, LDA first transformed to ice I_{sd} , then to ice I_c and eventually to ice Ih at 210 K. The same sequence of transformations, *viz.*, ice-VII \rightarrow HDA \rightarrow LDA $\rightarrow I_{sd}$ \rightarrow ice I_c \rightarrow ice Ih, was finally observed at a higher heating rate of 2–3 K/min. Additional time-resolved experiments at fixed temperatures show the intermediate HDA and LDA can be captured in prolonged times. At 86 K, HDA persisted and coexisted with ice VII and LDA up to 312 s. At 115 K, ice VII completely vanished after 100s, and only LDA remained after 418 s. At an even higher temperature of 131 K, the HDA converted quickly to LDA. Results from this series of isobaric–isothermal experiments clearly show the kinetic nature of the decompression transformations of metastable ice VII.

Evaluation of the relative intensity of the different phases provides essential information on the energetic and kinetic of the transformation. A duration time (τ) can be defined for each transformation process. For ice VII to HDA, τ is the time required to convert the precursor to the product by 50%. For HDA \rightarrow LDA, and LDA crystallization, τ is the persistence time of HDA (LDA), *i.e.*, the time between the first detection and disappearance of the precursor, HDA, or LDA. Logarithm plots of the duration time as a function of inverse temperature for the ice VII \rightarrow HDA (amorphization), HDA \rightarrow LDA, and LDA crystallization processes are compared in Figure 14. The

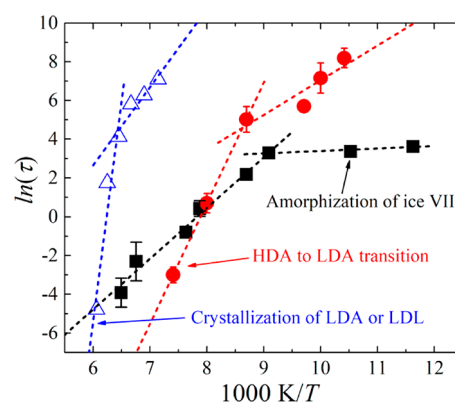


Figure 14. Arrhenius plots of the temperature dependence vs duration time (τ , in seconds) for the amorphization of ice VII, HDA–LDA transition, and crystallization of LDA. Adapted with permission from ref 40. Copyright 2020.

linear $\ln(\tau)$ versus $1/T$ relationships show the Arrhenius activation model is valid to describe the kinetics. For each transformation, there is a discontinuity between the two linear regions. The observation indicates that there are two distinct activation processes with different energy barriers involved. The slope of the linear fit provides information about the magnitude of the activation barrier. For example, below 110 K, the duration time for amorphization is almost independent of temperature. A fit to the Arrhenius equation yields an activation energy of 1.1(2) kJ/mol and a prefactor τ_0 of 8(3) s. The small activation energy and almost constant τ imply the

ice VII \rightarrow HDA transformation at ~ 5 mTorr is driven by a mechanical instability that requires little thermal activation. In contrast, above 110 K, the duration time of τ for the amorphization of ice VII varies exponentially with the temperature. In contrast to the fit to the Arrhenius equation, it is found that the duration time, τ , has shortened from ~ 27 s at 110 K to less than 20 ms at 154 K. Compared to the lower temperature regime (< 110 K), the activation barrier is 22(1) kJ/mol with τ_0 $7(1) \times 10^{-10}$ s. At high temperatures, the structural transformation, initiated by mechanical instability, occurs faster as the thermal energy further helps to promote it.

The Arrhenius plot of the HDA \rightarrow LDA transformation also shows a discontinuity at 115 K, which strongly suggests two mechanistic paths above and below this temperature. The temperature is remarkably close to the previously reported glass-transition temperature of HDA⁹⁸ that was interpreted as the crossover from nondiffusive motion to nanoscale diffusion in amorphous ice exhibiting a viscous liquid behavior. Isobaric–isothermal molecular dynamics (MD) decompression calculations have provided insight into the transformation in an atomic scale. The MD calculations succeeded in capturing the details of successive ice VII (modeled by hydrogen disordered ice VII) \rightarrow HDA \rightarrow LDA transformations. It is known from experiments that there is a volume increase of 30% when HDA is converted to LDA. The volume change translates to an $\sim 11\%$ increase in the linear dimension ($\sim \sqrt[3]{1.3}$) of the LDA structure. From previous diffraction studies, it is known that the volume expansion is due to the relaxation of the second nearest O–O coordination shell. Because the experimental second closest O–O distance in HDA is in the range of 3.5–4.5 Å, the second-nearest-neighbor oxygen atoms in LDA are displaced by 4–5 Å. The order-of-magnitude estimate agrees with the instantaneous oxygen-atom positions determined from the MD trajectory. Figure 15 shows the superimposition of the oxygen atom

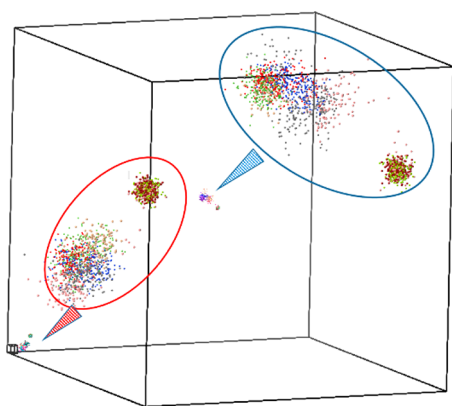


Figure 15. Evolution of the instantaneous oxygen atom positions plotted for two randomly selected water molecules within 1 ns during the decompression of ice VIII at 130 K enlarged in the ellipsoids. The other water molecules in the simulation model have been removed for clarity. The time trajectory is divided into three time segments of 3000 ps and represented by different colors. Within each circled region, the water initially vibrates with a confined space and then suddenly displaced, and the motion becomes more disperse because of the change in the density. Because the size of the simulation box changes with the transformation process, the atom positions were plotted in Cartesian coordinates. The outline of the simulation box serves only to illustrate the approximate dimension of the model. Adapted with permission from ref 40. Copyright 2020.

positions of two randomly selected water molecules within 1 ns at 130. Initially, the water molecules oscillate around their respective mean positions of ice VIII (indicated by the almost spherical distribution). When ice VIII structure is converted to HDA, there is a sudden displacement of the water atoms, as noted in the large amplitude movement of the atom positions. Over time, the structure transforms gradually to a lower-density form. The spatial “spread” of the water molecules becomes more extensive, as the water is seeking equilibrium positions in the voids formed by the volume expansion. The average atom displacement is about 10% of the cell length or around 5 Å (0.5 nm). The estimated atomic displacement is consistent with the recent measurement from the X-ray speckle experiment, showing the atom movement is in the nanometer range.⁹⁹

Summary. The few examples given exploring the crystalline and amorphous ice phase diagrams demonstrate the versatility of time-resolved X-ray diffraction at variable pressure and temperature. The combination can provide both kinetics and structural information in the time regime down to milliseconds. Systematic studies on ice show that in the water’s no man’s land, HDA can be transformed from ice Ih/Isd in the thermally stable pressure region of ice VI, while LDA forms from ice VIII in the stable pressure region of ice Ih. Both HDA and LDA occur as intermediate states in the crystalline–crystalline transition because of the lower kinetic barrier in “melting” than between the low-pressure and high-pressure crystalline phases. Time-resolved XRD results provide helpful information for theoretical prediction and explanation of liquid water’s anomalous behaviors. On the other hand, the persistence times of HDA and LDA as intermediate states depend on the temperature, decreasing exponentially with increasing temperature. For example, it is a few milliseconds for LDA at 165 K and HDA at 174 K. The persistence times are close to the time of homogeneous nucleation of supercooled liquid water at 227 K.⁸⁶ At higher temperatures, kinetically controlled “melting” of ice VIII and Ic into HDA and LDA will occur on a microsecond time scale, or even at a nanosecond time scale. An extensive temperature range (175–227 K) deep inside no man’s land is unreachable with the current dynamic compression technique and TRXRD detector because of the time constraint. There is still enormous opportunity to continue developing rapid compression/decompression techniques and faster 2D photon detectors to explore the transition dynamics in this (P, T) region.

Outlook. The millisecond/microsecond dynamic compression and TRXRD techniques can be used to explore other topics in the intermediate time scale regime. This Perspective presents only a few examples focusing on the dynamic kinetics of phase transitions in ice in the millisecond time scale regime. High-pressure nonequilibrium dynamics is an emerging field of research, particularly for underlying transition mechanism, synthesizing metastable materials with novel properties. A vast range of problems on the dynamics processes, such as time-dependent transition pathways, structural metastability, structural relaxation, displacive transformation, crystal morphology, and transient physical/electronic properties remain unexplored.

The time scale of millisecond and microsecond time compression/decompression is between static loading (longer than second) and shock wave experiments (nanosecond or shorter) (Figure 1). Because of experimental limitations, currently there is no unifying principle linking the evolution

of the dynamic kinetics for phase transition from shock to static compression. For example, in some materials, the change from thermally induced nucleation in static-compression to dislocation is still not understood. Information on the dynamic nonequilibrium process in the intermediate time scale regime is mandatory. Next, we discuss a few topics for future applications of dynamic compression and TRXRD.

The synthesis of metastable materials is one of the potential applications of dDAC.³⁹ Understanding the transition mechanism and formation conditions of metastable phases is crucial in materials science, condensed matter physics, and chemical synthesis. The heating/cooling rate can alter the kinetic path of the materials, and the compression/decompression rate can influence the transition pathway and may lead to a new metastable form. This is because the phase transition process is not only determined by the driving force but also is related to the transition kinetic barrier, loading rate, temperature, and other thermophysical factors. The current theoretical structure prediction techniques were primarily designed to explore only the stable thermodynamic structures.¹⁵ These methods are not suitable for predicting metastable structures. Furthermore, it cannot provide information on the transition kinetic path and the conditions to form the metastable state. The combination of TRXRD and dDAC is a powerful tool in the investigation of the structural evolution of materials at various conditions under compression/decompression with different rates, providing deep insight into the underlying transition mechanism and synthesis conditions of metastable states. Then what type of materials will exhibit time-dependent paths in the formation of metastable phases? In ice, static high-pressure experiments show diverse metastable phases and distinctive (thermally activated and kinetically driven) transition mechanisms. The loading rates significantly affect the transition processes when the compression time scale is close to the intrinsic structural relaxation determined by the energy and chemical bond barrier. It is expected that similar time-dependent phenomena will occur in SiO₂ and GeO₂, in which the phase diagrams exhibit diverse metastable phases with different transition mechanisms. Other system that may show time/temperature-dependence in the formation of metastable phases are semiconductors and elemental solids when the chemical bond property changes from covalent to metallic. For example, recent TRXRD experiments have shown two distinctive temperature- and rate-dependent pathways in the formation of metastable silicon phases, *viz.*, a thermally activated crystal–crystal transition from Si–II to a crystalline bc8/r8 phase under slow decompression and a mechanically driven amorphization under rapid decompression.³⁹ The experimental results show coupled effect of rate, temperature (thermal energy), and intrinsic activation barrier on the kinetic paths, which is of fundamental significance in controlled synthesis of the desirable metastable phases for practical use.

Dynamic experiments in the intermediate time scale can provide essential information on the kinetic energy barrier as a function of pressure. The kinetic barrier for a thermally induced phase transformation will change with external pressure. The structural phase transition often stagnates with the coexistence of two phases because of the grain interface, strain/stress energy, and surface energy. These factors all contribute to the new energy barriers. An additional driving force is required to promote the phase transition, *i.e.*, via dynamic compression/decompression. Previous studies on the

solid–solid transition of KCl have shown that both the transition pressure and effective energy barrier at a given temperature are related to the loading/unloading rates, following classical nucleation and growth theories.³⁰ Systematic studies of the rate-dependent transition kinetic processes at various temperatures could provide information about dynamic parameters for the transition with the energy barrier as a function of pressure in most materials.

To date, most time-resolved high-pressure investigations have focused on the study of structural transformation under rapid loading/unloading. Little work has been devoted to characterizing the physical and electronic properties, such as mechano-luminescence and piezoelectricity under nonequilibrium conditions.^{100,101} These phenomena are relevant to the conversion of mechanical energy to photon energy or electrical energy. Recently, Zhang et al., developed an advanced mechano-luminescence characterization system based on the dDAC to probe the mechano-luminescence of ZnS:Mn in the dDAC under dynamic compression/decompression at different loading/unloading rates.¹⁰¹ The mechano-luminescence intensity is dependent on the time-dependent pressure change. Another recent example is the strong photoluminescence induced by structural changes of the compressed heterostructured core/shell MnSe/MnS noncrystals that is maintained upon pressure release.¹⁰² These works present a new dimension in the use of the dDAC to manipulate the property in mechanoluminescent materials. Further research along a similar direction of energy conversion is highly desirable. The combination of dDAC and TRXRD is a powerful experimental technique to probe the mechanism and efficiency of the interconversion of pressure–volume work with other energy.

AUTHOR INFORMATION

Corresponding Author

John S. Tse – Department of Physics and Engineering Physics, University of Saskatchewan, Saskatoon, Saskatchewan S7N 5E2, Canada; orcid.org/0000-0001-8389-7615; Email: john.tse@usask.ca

Author

Chuanlong Lin – Center for High-Pressure Science and Technology Advanced Research, Beijing 100094, P.R. China

Complete contact information is available at: <https://pubs.acs.org/10.1021/acs.jpcllett.1c01623>

Notes

The authors declare no competing financial interest.

ACKNOWLEDGMENTS

The authors thank the beamline scientists at HPCAT (G. Shen, J.S. Smith, and S.V. Sinogeikin) and F. Zou CLS@APS for their continuing support. Synchrotron beam times were provided by Advanced Photon Source supported by the U.S. Department of Energy—Basic Energy Sciences and the Canadian Light Source and its funding partners. C.L. acknowledges funding from the National Nature Science Foundation of China (No.11974033), the Science Challenge Project (No. TZ2016001), and the Foundation of National Key Laboratory of Shockwave and Detonation Physics of China (No. 6142A03191002). The research is also supported by a NSERC Discovery Grant to J.S.T.

REFERENCES

- (1) Mao, H.-K.; Chen, X.-J.; Ding, Y.; Li, B.; Wang, L. Solids, liquids, and gases under high pressure. *Rev. Mod. Phys.* **2018**, *90* (1), 015007.
- (2) Tse, J. S. A chemical perspective on high pressure crystal structures and properties. *Nat. Sci. Rev.* **2020**, *7* (1), 149–169.
- (3) Hall, H. T.; Merrill, L.; Barnett, J. D. High Pressure Polymorphism in Cesium. *Science* **1964**, *146* (3649), 1297–1299.
- (4) Sternheimer, R. On the Compressibility of Metallic Cesium. *Phys. Rev.* **1950**, *78* (3), 235–243.
- (5) McMahon, M. I.; Nelmes, R. J.; Rekihi, S. Complex Crystal Structure of Cesium-III. *Phys. Rev. Lett.* **2001**, *87* (25), 255502.
- (6) von Schnering, H. G.; Nesper, R. How Nature Adapts Chemical Structures to Curved Surfaces. *Angew. Chem., Int. Ed. Engl.* **1987**, *26* (11), 1059–1080.
- (7) Jayaraman, A. Diamond anvil cell and high-pressure physical investigations. *Rev. Mod. Phys.* **1983**, *55* (1), 65–108.
- (8) Paszkowicz, W. High-pressure powder X-ray diffraction at the turn of the century. *Nucl. Instrum. Methods Phys. Res., Sect. B* **2002**, *198* (3), 142–182.
- (9) Hemley, R. J.; Mao, H.-k.; Struzhkin, V. V. Synchrotron radiation and high pressure: new light on materials under extreme conditions. *J. Synchrotron Radiat.* **2005**, *12* (2), 135–154.
- (10) Mao, H. K.; Mao, W. L. Theory and Practice – Diamond-Anvil Cells and Probes for High P–T Mineral Physics Studies. In *Treatise on Geophysics*; Schubert, G., Ed.; Elsevier: Amsterdam, 2007; pp 231–267.
- (11) Shen, G.; Mao, H. K. High-pressure studies with x-rays using diamond anvil cells. *Rep. Prog. Phys.* **2017**, *80*, 016101.
- (12) Bassett, W. A. Diamond anvil cell, 50th birthday. *High Pressure Res.* **2009**, *29* (2), 163–186.
- (13) Goncharov, A. F. Raman Spectroscopy at High Pressures. *Int. J. Spectrosc.* **2012**, *2012*, 617528.
- (14) McMahon, M. I.; Nelmes, R. J. High-pressure structures and phase transformations in elemental metals. *Chem. Soc. Rev.* **2006**, *35* (10), 943–963.
- (15) Oganov, A. R. Modern Methods of Crystal Structure Prediction. In *Modern Methods of Crystal Structure Prediction*; 2010.
- (16) Drozdov, A. P.; Erements, M. I.; Troyan, I. A.; Ksenofontov, V.; Shylin, S. I. Conventional superconductivity at 203 K at high pressures in the sulfur hydride system. *Nature* **2015**, *525* (7567), 73–76.
- (17) Drozdov, A. P.; Kong, P. P.; Minkov, V. S.; Besedin, S. P.; Kuzovnikov, M. A.; Mozaffari, S.; Balicas, L.; Balakirev, F. F.; Graf, D. E.; Prakapenka, V. B.; et al. Superconductivity at 250 K in lanthanum hydride under high pressures. *Nature* **2019**, *569* (7757), 528–531.
- (18) Snider, E.; Dasenbrock-Gammon, N.; McBride, R.; Debessai, M.; Vindana, H.; Vencatasamy, K.; Lawler, K. V.; Salamat, A.; Dias, R. P. Room-temperature superconductivity in a carbonaceous sulfur hydride. *Nature* **2020**, *586* (7829), 373–377.
- (19) Haberl, B.; Strobel, T. A.; Bradby, J. E. Pathways to exotic metastable silicon allotropes. *Appl. Phys. Rev.* **2016**, *3* (4), 040808.
- (20) Chapter 2 - Classification of Phase Transformations. In *Pergamon Materials Series*; Banerjee, S., Mukhopadhyay, P., Eds.; Pergamon, 2007; Vol. 12, pp 87–123.
- (21) Chandra Shekar, N. V.; Rajan, K. G. Kinetics of pressure induced structural phase transitions—A review. *Bull. Mater. Sci.* **2001**, *24* (1), 1–21.
- (22) McMahon, M. I. *Synchrotron and FEL Studies of Matter at High Pressures*; Jaeschke, E., Khan, S., Schneider, J. R., Hastings, J. B., Eds.; Springer International Publishing: Switzerland, 2020; 1857–1896.
- (23) Smith, J. S.; Sinogeikin, S. V.; Lin, C.; Rod, E.; Bai, L.; Shen, G. Developments in time-resolved high pressure x-ray diffraction using rapid compression and decompression. *Rev. Sci. Instrum.* **2015**, *86* (7), 072208.
- (24) Sinogeikin, S. V.; Smith, J. S.; Rod, E.; Lin, C.; Kenney-Benson, C.; Shen, G. Online remote control systems for static and dynamic compression and decompression using diamond anvil cells. *Rev. Sci. Instrum.* **2015**, *86* (7), 072209.
- (25) Luo, B. Q.; Chen, X. M.; Wang, G. J.; Tan, F. L.; Chen, G. H.; Zhao, J. H.; Sun, C. W. Dynamic strength measurement of aluminum under magnetically driven ramp wave pressure-shear loading. *Int. J. Impact Engineering* **2017**, *100*, 56–61.
- (26) Evans, W. J.; Yoo, C.-S.; Lee, G. W.; Cynn, H.; Lipp, M. J.; Visbeck, K. Dynamic diamond anvil cell (dDAC): A novel device for studying the dynamic-pressure properties of materials. *Rev. Sci. Instrum.* **2007**, *78* (7), 073904.
- (27) Jenei, Z.; Liermann, H. P.; Husband, R.; Méndez, A. S. J.; Pennicard, D.; Marquardt, H.; O'Bannon, E. F.; Pakhomova, A.; Konopkova, Z.; Glazyrin, K.; et al. New dynamic diamond anvil cells for tera-pascal per second fast compression x-ray diffraction experiments. *Rev. Sci. Instrum.* **2019**, *90* (6), 065114.
- (28) Cheng, H.; Zhang, J.; Li, Y.; Li, G.; Li, X.; Liu, J. A convenient dynamic loading device for studying kinetics of phase transitions and metastable phases using symmetric diamond anvil cells. *High Pressure Res.* **2018**, *38* (1), 32–40.
- (29) Liermann, H. P.; Konopkova, Z.; Appel, K.; Prescher, C.; Schropp, A.; Cerantola, V.; Husband, R. J.; McHardy, J. D.; McMahon, M. I.; McWilliams, R. S.; et al. Novel experimental setup for megahertz X-ray diffraction in a diamond anvil cell at the High Energy Density (HD) instrument of the European X-ray Free-Electron Laser (EuXFEL). *J. Synchrotron Radiat.* **2021**, *28*, 688–706.
- (30) Lin, C.; Smith, J. S.; Sinogeikin, S. V.; Park, C.; Kono, Y.; Kenney-Benson, C.; Rod, E.; Shen, G. Kinetics of the B1-B2 phase transition in KCl under rapid compression. *J. Appl. Phys.* **2016**, *119* (4), 045902.
- (31) Méndez, A. S. J.; Marquardt, H.; Husband, R. J.; Schwark, I.; Mainberger, J.; Glazyrin, K.; Kurnosov, A.; Otzen, C.; Satta, N.; Bednarcik, J.; et al. A resistively-heated dynamic diamond anvil cell (RHdDAC) for fast compression x-ray diffraction experiments at high temperatures. *Rev. Sci. Instrum.* **2020**, *91* (7), 073906.
- (32) Lee, G. W.; Evans, W. J.; Yoo, C.-S. Crystallization of water in a dynamic diamond-anvil cell: Evidence for ice VII-like local order in supercompressed water. *Phys. Rev. B: Condens. Matter Mater. Phys.* **2006**, *74* (13), 134112.
- (33) Méndez, A. S. J.; Trybel, F.; Husband, R. J.; Steinle-Neumann, G.; Liermann, H. P.; Marquardt, H. Bulk modulus of H₂O across the ice VII–ice X transition measured by time-resolved x-ray diffraction in dynamic diamond anvil cell experiments. *Phys. Rev. B: Condens. Matter Mater. Phys.* **2021**, *103* (6), 064104.
- (34) Jia, R.; Shao, C. G.; Su, L.; Huang, D. H.; Liu, X. R.; Hong, S. M. Rapid compression induced solidification of bulk amorphous sulfur. *J. Phys. D: Appl. Phys.* **2007**, *40* (12), 3763–3766.
- (35) Yu, P.; Wang, W. H.; Wang, R. J.; Lin, S. X.; Liu, X. R.; Hong, S. M.; Bai, H. Y. Understanding exceptional thermodynamic and kinetic stability of amorphous sulfur obtained by rapid compression. *Appl. Phys. Lett.* **2009**, *94* (1), 011910.
- (36) Chen, J.-Y.; Yoo, C.-S. High density amorphous ice at room temperature. *Proc. Natl. Acad. Sci. U. S. A.* **2011**, *108* (19), 7685–7688.
- (37) Lin, C.; Smith, J. S.; Sinogeikin, S. V.; Shen, G. Experimental evidence of low-density liquid water upon rapid decompression. *Proc. Natl. Acad. Sci. U. S. A.* **2018**, *115* (9), 2010–2015.
- (38) Lin, C.; Smith, J. S.; Liu, X.; Tse, J. S.; Yang, W. Venture into water's No Man's land: Structural transformations of solid H₂O under rapid compression and decompression. *Phys. Rev. Lett.* **2018**, *121* (22), 225703.
- (39) Lin, C.; Liu, X.; Yang, D.; Li, X.; Smith, J. S.; Wang, B.; Dong, H.; Li, S.; Yang, W.; Tse, J. S. Temperature- and Rate-Dependent Pathways in Formation of Metastable Silicon Phases under Rapid Decompression. *Phys. Rev. Lett.* **2020**, *125* (15), 155702.
- (40) Lin, C.; Liu, X.; Yong, X.; Tse, J. S.; S. Smith, J.; J. English, N.; Wang, B.; Li, M.; Yang, W.; Mao, H.-K. Temperature-dependent kinetic pathways featuring distinctive thermal-activation mechanisms in structural evolution of ice VII. *Proc. Natl. Acad. Sci. U. S. A.* **2020**, *117* (27), 15437–15442.
- (41) Kim, Y.-J.; Lee, Y.-H.; Lee, S.; Nada, H.; Lee, G. W. Shock growth of ice crystal near equilibrium melting pressure under dynamic

- compression. *Proc. Natl. Acad. Sci. U. S. A.* **2019**, *116* (18), 8679–8684.
- (42) Shi, K.; Liu, B.; Wu, Y.; Liang, Z.; Wang, X.; Su, L.; Wang, Y.; Zhang, L.; Yang, G.; Zhang, Y.; et al. In-Situ Observation of the Formation of Fibrous Sulfur under High Pressure. *J. Phys. Chem. C* **2019**, *123* (23), 14696–14700.
- (43) Lee, G. W.; Evans, W. J.; Yoo, C.-S. Dynamic pressure-induced dendritic and shock crystal growth of ice VI. *Proc. Natl. Acad. Sci. U. S. A.* **2007**, *104* (22), 9178–9181.
- (44) Tomasino, D.; Yoo, C.-S. Solidification and crystal growth of highly compressed hydrogen and deuterium: Time-resolved study under ramp compression in dynamic-diamond anvil cell. *Appl. Phys. Lett.* **2013**, *103* (6), 061905.
- (45) Chen, J.-Y.; Yoo, C.-S.; Evans, W. J.; Liermann, H.-P.; Cynn, H.; Kim, M.; Jenei, Z. Solidification and fcc to metastable hcp phase transition in krypton under variable compression rates. *Phys. Rev. B: Condens. Matter Mater. Phys.* **2014**, *90* (14), 144104.
- (46) Zhang, L.; Shi, K.; Wang, Y.; Kong, J.; Qiao, P.; Yang, H.; Zhang, J.; Su, L.; Dong, X.; Yang, G. Compression Rate-Dependent Crystallization of Pyridine. *J. Phys. Chem. C* **2021**, *125* (12), 6983–6989.
- (47) Chen, J.-Y.; Yoo, C.-S. Formation and phase transitions of methane hydrates under dynamic loadings: Compression rate dependent kinetics. *J. Chem. Phys.* **2012**, *136* (11), 114513.
- (48) Konôpková, Z.; Rothkirch, A.; Singh, A. K.; Speziale, S.; Liermann, H.-P. In situ x-ray diffraction of fast compressed iron: Analysis of strains and stress under non-hydrostatic pressure. *Phys. Rev. B: Condens. Matter Mater. Phys.* **2015**, *91* (14), 144101.
- (49) Lin, C.; Yong, X.; Tse, J. S.; Smith, J. S.; Sinogeikin, S. V.; Kenney-Benson, C.; Shen, G. Kinetically Controlled Two-Step Amorphization and Amorphous-Amorphous Transition in Ice. *Phys. Rev. Lett.* **2017**, *119* (13), 135701.
- (50) Hiraio, N.; Kawaguchi, S. I.; Hirose, K.; Shimizu, K.; Ohtani, E.; Ohishi, Y. New developments in high-pressure X-ray diffraction beamline for diamond anvil cell at SPring-8. *Matter Radiat. Extremes* **2020**, *5* (1), 018403.
- (51) Shen, G.; Chow, P.; Xiao, Y.; Sinogeikin, S.; Meng, Y.; Yang, W.; Liermann, H.-P.; Shebanova, O.; Rod, E.; Bommannavar, A.; et al. HPCAT: an integrated high-pressure synchrotron facility at the Advanced Photon Source. *High Pressure Res.* **2008**, *28* (3), 145–162.
- (52) Liermann, H.-P.; Konopkova, Z.; Morgenroth, W.; Glazyrin, K.; Bednarcik, J.; McBride, E. E.; Petitgirard, S.; Delitz, J. T.; Wendt, M.; Bican, Y.; et al. The Extreme Conditions Beamline P02.2 and the Extreme Conditions Science Infrastructure at PETRA III. *J. Synchrotron Radiat.* **2015**, *22* (4), 908–924.
- (53) Shen, G.; Wang, Y. High-pressure Apparatus Integrated with Synchrotron Radiation. *Rev. Mineral. Geochem.* **2014**, *78* (1), 745–777.
- (54) Liu, J. High pressure x-ray diffraction techniques with synchrotron radiation. *Chin. Phys. B* **2016**, *25* (7), 076106.
- (55) McMahon, M. I. *Synchrotron and FEL Studies of Matter at High Pressures*. 2020; Jaeschke, E., Khan, S., Schneider, J. R., Hastings, J. B., Eds.; Springer International Publishing: Switzerland, 2020; 1857–1896; Argonne National Lab. (ANL), Argonne, IL (United States). Advanced Photon Source (APS).
- (56) Wang, X.; Rigg, P.; Sethian, J.; Sinclair, N.; Weir, N.; Williams, B.; Zhang, J.; Hawreliak, J.; Toyoda, Y.; Gupta, Y.; et al. The laser shock station in the dynamic compression sector. I. *Rev. Sci. Instrum.* **2019**, *90* (5), 053901.
- (57) Singh, A. K. The Kinetics of some Pressure-Induced Transformations. *Mater. Sci. Forum* **1985**, *3*, 291–306.
- (58) Glasstone, S.; Laidler, K. J.; Eyring, H. *Theory of Rate Processes*; McGraw-Hill: New York, 1941.
- (59) Christian, J. W. *The Theory of Transformation in Metals and Alloys*; Pergamon: Oxford, 2002.
- (60) Fanfoni, M.; Tomellini, M. The Johnson-Mehl-Avrami-Kohnogorov model: A brief review. *Nuovo Cimento Soc. Ital. Fis., D* **1998**, *20* (7), 1171–1182.
- (61) Porter, D. A.; Easterling, K. E.; Sherif, M. Y. *Phase transformations in metals and alloys*, 3rd ed.; CRC Press: New York, 2009.
- (62) Levitas, V. I.; Henson, B. F.; Smilowitz, L. B.; Asay, B. W. Solid-Solid Phase Transformation via Virtual Melting Significantly Below the Melting Temperature. *Phys. Rev. Lett.* **2004**, *92* (23), 235702.
- (63) Levitas, V. I. Crystal-Amorphous and Crystal-Crystal Phase Transformations via Virtual Melting. *Phys. Rev. Lett.* **2005**, *95* (7), 075701.
- (64) Lin, C.; Smith, J. S.; Sinogeikin, S. V.; Kono, Y.; Park, C.; Kenney-Benson, C.; Shen, G. A metastable liquid melted from a crystalline solid under decompression. *Nat. Commun.* **2017**, *8* (1), 14260.
- (65) Peng, Y.; Wang, F.; Wang, Z.; Alsayed, A. M.; Zhang, Z.; Yodh, A. G.; Han, Y. Two-step nucleation mechanism in solid–solid phase transitions. *Nat. Mater.* **2015**, *14* (1), 101–108.
- (66) Pogatscher, S.; Leutenegger, D.; Schawe, J. E. K.; Uggowitzer, P. J.; Löffler, J. F. Solid–solid phase transitions via melting in metals. *Nat. Commun.* **2016**, *7* (1), 11113.
- (67) Ysautomi, M. *The Physics of Liquid*; CRC Press, Taylor and Francis, 2021.
- (68) Tse, J. S.; Klug, D. D. Pressure amorphized ices – an atomistic perspective. *Phys. Chem. Chem. Phys.* **2012**, *14* (23), 8255–8263.
- (69) Mishima, O. Relationship between melting and amorphization of ice. *Nature* **1996**, *384* (6609), 546–549.
- (70) Mishima, O.; Stanley, H. E. The relationship between liquid, supercooled and glassy water. *Nature* **1998**, *396* (6709), 329–335.
- (71) Mishima, O. Volume of supercooled water under pressure and the liquid-liquid critical point. *J. Chem. Phys.* **2010**, *133* (14), 144503.
- (72) Mishima, O.; Calvert, L. D.; Whalley, E. ‘Melting ice’ I at 77 K and 10 kbar: a new method of making amorphous solids. *Nature* **1984**, *310* (5976), 393–395.
- (73) Loerting, T.; Salzmann, C.; Kohl, I.; Mayer, E.; Hallbrucker, A. A second distinct structural “state” of high-density amorphous ice at 77 K and 1 bar. *Phys. Chem. Chem. Phys.* **2001**, *3* (24), 5355–5357.
- (74) Mishima, O.; Calvert, L. D.; Whalley, E. An apparently first-order transition between two amorphous phases of ice induced by pressure. *Nature* **1985**, *314* (6006), 76–78.
- (75) Tulk, C. A.; Benmore, C. J.; Urquidí, J.; Klug, D. D.; Neuefeind, J.; Tomberli, B.; Egelstaff, P. A. Structural Studies of Several Distinct Metastable Forms of Amorphous Ice. *Science* **2002**, *297* (5585), 1320–1323.
- (76) Nemes, R. J.; Loveday, J. S.; Strässle, T.; Bull, C. L.; Guthrie, M.; Hamel, G.; Klotz, S. Annealed high-density amorphous ice under pressure. *Nat. Phys.* **2006**, *2* (6), 414–418.
- (77) Gallo, P.; Amann-Winkel, K.; Angell, C. A.; Anisimov, M. A.; Caupin, F.; Chakravarty, C.; Lascaris, E.; Loerting, T.; Panagiotopoulos, A. Z.; Russo, J.; et al. Water: A Tale of Two Liquids. *Chem. Rev.* **2016**, *116* (13), 7463–7500.
- (78) Amann-Winkel, K.; Böhmer, R.; Fujara, F.; Gainaru, C.; Geil, B.; Loerting, T. Colloquium: Water’s controversial glass transitions. *Rev. Mod. Phys.* **2016**, *88* (1), 011002.
- (79) Fisher, K.; Devlin, J. P. Defect activity in amorphous ice from isotopic exchange data: insight into the glass transition. *J. Phys. Chem.* **1995**, *99*, 11584–11590.
- (80) Shephard, J. J.; Salzmann, C. G. Molecular Reorientation dynamics govern the glass transitions of the amorphous ices. *J. Phys. Chem. Lett.* **2016**, *7*, 2281–2285.
- (81) Poole, P. H.; Sciortino, F.; Essmann, U.; Stanley, H. E. Phase behaviour of metastable water. *Nature* **1992**, *360* (6402), 324–328.
- (82) Stanley, H. E.; Buldyrev, S. V.; Canpolat, M.; Mishima, O.; Sadr-Lahijany, M. R.; Scala, A.; Starr, F. W. The puzzling behavior of water at very low temperature. Invited Lecture. *Phys. Chem. Chem. Phys.* **2000**, *2* (8), 1551–1558.
- (83) Klotz, S.; Hamel, G.; Loveday, J. S.; Nemes, R. J.; Guthrie, M. Recrystallisation of HDA ice under pressure by in-situ neutron diffraction to 3.9 GPa. *Z. Kristallogr. - Cryst. Mater.* **2003**, *218* (2), 117–122.

- (84) Klotz, S.; Strässle, T.; Saitta, A. M.; Rousse, G.; Hamel, G.; Nelmes, R. J.; Loveday, J. S.; Guthrie, M. In situ neutron diffraction studies of high density amorphous ice under pressure. *J. Phys.: Condens. Matter* **2005**, *17* (11), S967–S974.
- (85) Mishima, O.; Suzuki, Y. Vitrification of emulsified liquid water under pressure. *J. Chem. Phys.* **2001**, *115* (9), 4199–4202.
- (86) Sellberg, J. A.; Huang, C.; McQueen, T. A.; Loh, N. D.; Laksmo, H.; Schlesinger, D.; Sierra, R. G.; Nordlund, D.; Hampton, C. Y.; Starodub, D.; et al. Ultrafast X-ray probing of water structure below the homogeneous ice nucleation temperature. *Nature* **2014**, *510* (7505), 381–384.
- (87) Tse, J. S.; Klein, M. L. Pressure induced amorphization of ice Ih. *J. Chem. Phys.* **1990**, *92* (6), 3992–3994.
- (88) Tse, J. S.; Klug, D. D.; Tulk, C. A.; Swainson, I.; Svensson, E. C.; Loong, C. K.; Shpakov, V.; Belosludov, V. R.; Belosludov, R. V.; Kawazoe, Y. The mechanisms for pressure-induced amorphization of ice Ih. *Nature* **1999**, *400* (6745), 647–649.
- (89) English, N. J.; Tse, J. S. Reversible pressure-induced crystal-amorphous structural transformation in ice Ih. *Chem. Phys. Lett.* **2014**, *609*, 54–58.
- (90) Tse, J. S. Mechanical instability in ice Ih. A mechanism for pressure-induced amorphization. *J. Chem. Phys.* **1992**, *96* (7), 5482–5487.
- (91) Strässle, T.; Saitta, A. M.; Klotz, S.; Braden, M. Phonon Dispersion of Ice under Pressure. *Phys. Rev. Lett.* **2004**, *93* (22), 225901.
- (92) Hobbs, P. *Ice Physics*; Oxford University Press, 1974.
- (93) Tulk, C. A.; Molaison, J. J.; Makhlof, A. R.; Manning, C. E.; Klug, D. D. Absence of amorphous forms when ice is compressed at low temperature. *Nature* **2019**, *569* (7757), 542–545.
- (94) Bauer, R.; Tse, J. S.; Komatsu, K.; Machida, S.; Hattori, T. Slow compression of crystalline ice at low temperature. *Nature* **2020**, *585* (7825), E9–E10.
- (95) Klug, D. D.; Handa, Y. P.; Tse, J. S.; Whalley, E. Transformation of ice VIII to amorphous ice by “melting” at low temperature. *J. Chem. Phys.* **1989**, *90* (4), 2390–2392.
- (96) Shephard, J. J.; Klotz, S.; Vickers, M.; Salzmänn, C. G. A new structural relaxation pathway of low-density amorphous ice. *J. Chem. Phys.* **2016**, *144* (20), 204502.
- (97) Tse, J. S.; Shpakov, V. P.; Belosludov, V. R. Vibrational spectrum, elastic moduli and mechanical stability in ice VIII. *J. Chem. Phys.* **1999**, *111* (24), 11111–11116.
- (98) Amann-Winkel, K.; Gainaru, C.; Handle, P. H.; Seidl, M.; Nelson, H.; Böhmer, R.; Loerting, T. Water’s second glass transition. *Proc. Natl. Acad. Sci. U. S. A.* **2013**, *110* (44), 17720–17725.
- (99) Perakis, F.; Amann-Winkel, K.; Lehmkuhler, F.; Sprung, M.; Mariedahl, D.; Sellberg, J. A.; Pathak, H.; Späh, A.; Cavalca, F.; Schlesinger, D.; et al. Diffusive dynamics during the high-to-low density transition in amorphous ice. *Proc. Natl. Acad. Sci. U. S. A.* **2017**, *114* (31), 8193–8198.
- (100) Wang, X.; Que, M.; Chen, M.; Han, X.; Li, X.; Pan, C.; Wang, Z. L. Full Dynamic-Range Pressure Sensor Matrix Based on Optical and Electrical Dual-Mode Sensing. *Adv. Mater.* **2017**, *29* (15), 1605817.
- (101) Zhang, L.; Shi, K.; Wang, Y.; Su, L.; Yang, G.; Huang, B.; Kong, J.; Dong, X.; Wang, Z. L. Unraveling the anomalous mechanoluminescence intensity change and pressure-induced red-shift for manganese-doped zinc sulfide. *Nano Energy* **2021**, *85*, 106005.
- (102) Wang, Y.; Liu, H.; Wu, M.; Wang, K.; Sui, Y.; Liu, Z.; Lu, S.; Nie, Z.; Tse, J. S.; Yang, X.; et al. New-phase retention in colloidal core/shell nanocrystals via pressure-modulated phase engineering. *Chem. Sci.* **2021**, *12*, 6580–6587.